Available online at www.sciencedirect.com
ScienceDirect
Advances in Water Resources 30 (2007) 301–313
Advances in Water Resources
www.elsevier.com/locate/advwatres

Hydrodynamics of coupled flow above and below a sediment–water interface with triangular bedforms

M. Bayani Cardenas [a,b,*], J.L. Wilson [a]

[a] Department of Earth and Environmental Science, New Mexico Institute of Mining and Technology, Socorro, NM 87801, United States
[b] Jackson School of Geosciences, Department of Geological Sciences, The University of Texas at Austin, Austin, TX 78712, United States

Received 20 December 2005; received in revised form 10 May 2006; accepted 26 June 2006
Available online 1 September 2006

Abstract

The hydrodynamics of a system where there is a coupled flow above and below a sediment–water interface (SWI) are not completely understood. We numerically simulate mean two-dimensional, unidirectional, steady, viscous flow in these systems using a sequentially coupled formulation. Simulations were conducted to determine fundamental relationships between bedform geometry, Reynolds number for the water-column flow (Re), interfacial exchange zone depth (d_z) in the sediments, and flux through the SWI (q_{int}); the latter two parameters play a significant role in biogeochemical and aquatic-life processes across the SWI. d_z and Re are functionally related through an asymptotic growth-curve model while q_{int} and Re follow a power function. These relationships are dynamically explained by the manner in which pressure gradients along the SWI develop due to current–bedform interactions at different Res and by Darcy's Law. We found that the coupling between water column and exchange zone flow is controlled by the behavior of the water-column eddy. The eddy detaches at or near the point of minimum pressure along the interface, and reattaches near the point of maximum pressure. These two critical points determine the pressure gradient along the bed surface that controls the exchange zone flow field. Moreover, the reattachment point corresponds to flow divides within the sediments. Lastly, pore-water velocities drop with depth below the SWI, and are larger below the bedform crests than below the troughs.

Keywords: Hyporheic zone; Sediment–water interface; Bedform; Navier-Stokes; Stream–aquifer interaction; FEMLAB

1. Introduction

1.1. Relevance and previous work

The physical and biogeochemical complexity of the sediment–water interface (SWI) or transition zone between benthic water and pore water, sometimes referred to as the "hyporheic zone" in freshwater aquatic systems, has not been investigated in detail. However, we know that ecologically and environmentally significant processes occurring in these zones control the distribution of solutes, colloids, dissolved gases and biogeochemical reactions from ripple to global scales [3,11,17,18,23,31,33,35,38,50], and thus affect the distribution of benthic flora and fauna in lakes, oceans, bays and estuaries [7,17,35], as well as hyporheic and riparian organisms in fluvial systems [14,15,46].

While field and laboratory observations are necessary for a comprehensive understanding of interfacial exchange processes, fundamental advancements are made when these empirical data are verified or reproduced through mathematical modeling based on the conservation laws of mass, momentum, and energy. Many studies have presented both modeled and observed results on fluid flow and solute transport for benthic-pore water exchange. These are reviewed in Boudreau [2], Jorgensen and Boudreau [22], and Huettel and Webster [19] for marine settings, and by Packman and Bencala [32] for fluvial hyporheic zones.

* Corresponding author. Address: Department of Earth and Environmental Science, New Mexico Institute of Mining and Technology, Socorro, NM 87801, United States. Tel.: +1 505 8355484.
E-mail address: cardenas@nmt.edu (M.B. Cardenas).

0309-1708/$ - see front matter © 2006 Elsevier Ltd. All rights reserved.
doi:10.1016/j.advwatres.2006.06.009

There is no specific marine counterpart for the freshwater 'hyporheic zone', thus we generalize the nomenclature and refer instead to the interfacial exchange zone (IEZ) as the volume within the permeable sediments that is physically influenced by fluid exchange across the sediment–water interface.

A holistic view of the dynamics of the IEZ necessarily begins with a comprehensive knowledge of the fluid physics as mass flux is usually governed by advection rather than molecular diffusion or dispersion [17,40]. Advective exchange between the water column and the underlying porous sediments occurs mainly due to pressure gradients. These pressure gradients are typically generated by currents above any bed-surface topography or by oscillatory flow due to waves and tidal fluctuations [19,42,49]. Some benthic organisms also generate flow across the sediment–water interface and mixing of sediments; these phenomena are referred to as bioirrigation and bioturbation. Aside from the advective process, which has been referred to as "pumping", the movement of bedforms also results in the trapping and release of solutes and is termed "turnover" [11]. A thorough investigation of the mechanics of pumping is necessary if we are to understand the fluid physics of IEZs.

Several studies, often supported by experiments, have investigated the mechanics of pumping but within a limited context. Most studies focus on the sediments and assume that the water-column bottom pressure (the sediment's top boundary condition) is given *ab extra*. Thibodeaux and Boyle [45] present results of flume experiments with gravel beds and apply Darcy's Law, combined with pressure distributions measured over triangular roughness from Vittal et al. [48], to estimate pore-water velocities along the SWI. This study illustrated the presence of interfacial exchange but did not thoroughly investigate the fundamental hydrodynamics of the system either in the water column or within the sediments. Savant et al. [40], applying the boundary element numerical method, replicate flume observations of flow through a single dune induced by pressure gradients, which were also calculated following Vittal et al. [48]. Elliott and Brooks [11] followed the same procedure of taking pressure profiles from previous experiments, this time from Fehlman [13], and imposed it as a boundary for a numerical model of Darcy flow within the sediments. Moreover, they approximated the pressure profile along the SWI with a sine function to derive an exact solution for potential flow in the sediments, while assuming that the interface is flat [11]. Observed tracer trajectories within permeable sediments were modeled successfully by Huettel and Gust [21] who applied a sink-source potential flow model. Although early numerical simulations of flow within the sediments considered bedform geometry explicitly [10,40], several recent approaches impose a functional pressure distribution on the flat upper boundary of pore-water flow models which consider homogeneous [18,31,42] as well as heterogeneous permeability fields [4,39]. The spatially periodic, and approximately sinusoidal, pressure distributions represent the impact of bed topography. Despite elucidating processes operating in the sediments, models that ignore the geometry of bedforms miss a substantial part of the IEZ and provide an incomplete picture. Marion et al. [24] have shown that pore-water flow models of pumping induced exchange with flat upper boundaries cannot accurately predict results of experiments when bedforms protrude significantly into the water column, i.e., bedform height is comparable to water-column depth. They attribute this to inadequate representation of the parts of dunes located higher than the mean bed elevation. Moreover, flume studies using gravel and sand beds show that pore-water flow velocities decelerate non-linearly away from the interface [20,30,45] supporting the emphasis on processes occurring along and adjacent to the bed surface.

The studies cited in the previous paragraph illustrated or emphasized processes within the sediments. There have been investigations that simultaneously analyze the flow above and below the interface. Ho and Gelhar [16] present results of analytical and experimental studies on turbulent flow in pipes with permeable walls characterized by wavy periodic topography. They assumed inviscid, irrotational flow in the water column, and thus had potential flow both within and above the permeable media. Shum [42] examines the effects of the passage of progressive gravity waves on advective transport in a porous rippled bed. Once again, potential flow was assumed for the oscillatory flow in the water column. This allowed for an exact representation of the pressure along the surface of the sinusoidal ripples and the derivation of an analytic solution for potential flow within the ripples. Furthermore, Shum [42] refers to unpublished numerical simulations of the Navier-Stokes equations for laminar oscillatory flow above the ripples. He also imposed this pressure solution as a boundary along the ripples for the flow model in the sediments. This allowed, for the first time, an investigation of the underlying and fundamental dynamics of advective exchange between rippled sediments and a water column driven by gravity waves. However, only a handful of cases were presented by Shum [42] and the study was limited to sinusoidal ripples under oscillatory flow. To our knowledge no similar study of pumping has been done for triangular bedforms under unidirectional flow. We address this gap through sequentially coupled numerical modeling of fluid flow both above and below a SWI with triangular bedform topography.

1.2. Purpose of this study

The goal of this paper is to use two-dimensional coupled flow simulations to elucidate the basic hydrodynamic interactions between mean unidirectional laminar flow in the water column above triangular bedforms, with porous flow in the underlying permeable sediments. The effects of oscillatory flow, turbulence, bioirrigation, and bioturbation are assumed negligible. Our audience is interdisciplinary scien-

tists concerned with the biogeochemistry and aquatic life of interfacial exchange zones. We address the following questions. How do bedforms affect water-column eddy geometry and the pressure distribution at the SWI? How do eddy geometry and the bottom pressure distribution affect interfacial exchange and flow through the underlying sediments? How do these effects change with flow conditions in the overlying water column and with bedform shape? These questions can also be posed for different scenarios of ambient groundwater discharge – 'neutral', 'gaining', or 'losing' conditions. The gaining scenario refers to cases where the water column is gaining net water, e.g., gaining rivers or lakes and coastal zones subjected to submarine groundwater discharge. The gaining case is addressed in another paper [5]. The reference case, where the water column is 'neutral' – neither gaining nor losing net water, is addressed here.

Among our assumptions the weakest is viscous (laminar) flow in the water column; in most natural systems this flow is turbulent. We felt it prudent to first examine a canonical situation, although still maintaining the geometric complexity of the bedform. An inviscid, irrotational model of the water column would not capture the separation and eddy that we later show controls interfacial exchange. The simplest flow field to do so involves viscous flow. A viscous modeling approach significantly increases our insight into interfacial exchange, leads to limiting conditions of interest in turbulent flows, and even has direct application to those few natural situations (lakes, wetlands, and some ocean bottoms) where laminar flow conditions exist. Throughout the development of hydrodynamics viscous-flow studies have played this pioneering role. Unlike turbulent flow, accurate solutions of the viscous-flow equations are easily achieved with minimal approximation, as we do using computational fluid dynamics. Shum's [42] study, discussed above, is an example where a laminar-flow-based investigation provided fundamental insight.

A recent special issue of *Advances in Water Resources* highlighted papers dealing with modeling of hyporheic zone processes [37] but included none that tackle the coupled hydrodynamics of the water column and porous sediments, not even for laminar-flow settings. Consideration for turbulent conditions (e.g., direct numerical solution of transient Navier-Stokes equations, large-scale Eddy Simulation, or Reynold's average approaches) is left for future studies.

2. Methodology

In order to answer our questions, we used FEMLAB, a multiphysics finite element analysis software, to numerically model the coupled flow in two-dimensions and at steady-state. The code solves the Navier-Stokes (NS) and continuity equations for incompressible flow for the water column:

$$\rho\frac{\partial \mathbf{u}}{\partial t} - \mu\nabla^2\mathbf{u} + \rho(\mathbf{u}\cdot\nabla)\mathbf{u} + \nabla p = 0 \tag{1}$$

$$\nabla\cdot\mathbf{u} = 0 \tag{2}$$

where ρ is the fluid density, $\mathbf{u}$ the velocity vector, μ the dynamic viscosity, and p is the dynamic pressure. Because of the choice of boundary conditions (below) this is effectively an "enclosed flow" problem. An enclosed system is one that is surrounded by fixed boundaries (as in these simulations) or that has a flow field of such spatial extent as to be considered infinite (as in application of the model results to, e.g., the ocean bottom). Total pressure is the sum of a hydrostatic pressure and the variable dynamic pressure, p. There is no need to represent gravity explicitly in (1) or in the porous bed domain, which is governed by the combination of Darcy's Law and the continuity equation for incompressible flow in a non-deformable media, i.e., the groundwater flow equation:

$$\nabla\cdot\mathbf{q} = 0 \tag{3}$$

$$\mathbf{q} = -\frac{k}{\mu}\nabla p \tag{4}$$

Here $\mathbf{q}$ is the specific discharge (i.e. Darcy "velocity") and k is intrinsic permeability. Direct solvers from the UMFPACK algorithm [9] are implemented in FEMLAB (now called COMSOL Multiphysics). Sequential coupling is implemented via imposing the NS-continuity derived pressure distribution along the bed surface as a Dirichlet boundary for the groundwater flow equation. The top of the water column is treated as a no-flow symmetry boundary and not as a free surface (Fig. 1a). The water column's bottom boundary, the sediment–water interface (SWI), assumes the no-slip/no-flow condition:

$$\mathbf{u} = 0 \tag{5}$$

The lower boundary of the porous domain is considered impermeable.

As already mentioned, the top (SWI) boundary of the porous domain is a prescribed pressure boundary derived from solving the NS equations in the water-column domain. Thus, by definition pressure is continuous across the two domains. However, although the NS velocity is zero at the SWI, the porous bed Darcy velocity is finite resulting in a discontinuous velocity distribution across the interface. Velocity jumps are common in porous systems with sharp contrasts in permeability, such as along the transition from clay to gravel. However, our sequential formulation results in a slight mass imbalance as fluxes into and out of the SWI are not accounted for in the water column. Our coupling is only one-way and not iterative. This imbalance is negligible for the water column as fluid fluxes through the SWI are miniscule compared to other water-column fluxes (less than 0.01% of flux through the water column). It is a somewhat awkward yet convenient approximation for the coupled interface (more on this later). Although formulations that ensure mass balance are possible (e.g., Brinkman-type or Beavers–Joseph-type equations), they are currently difficult to implement as they require *a priori* knowledge of additional parameters (effective viscosity in Brinkman-type equations and a slip-velocity in the Beavers–Joseph-type equations) and have been

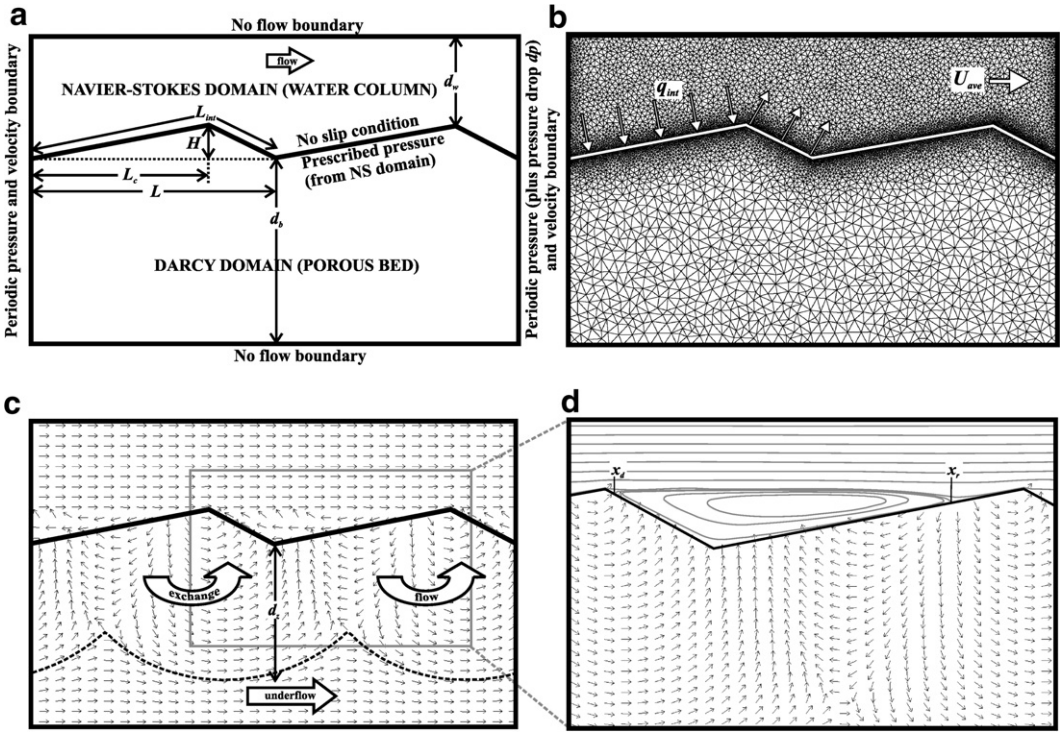

Fig. 1. (a) Schematic of model domain and system formulation. (b) Representative finite element mesh illustrating normal flux (small white arrows) through the bed surface, q_{int}, and average horizontal velocity in the water column (large white arrow), U_{ave}. (c) Typical solution for flow directions (arrows are of equal lengths and do not indicate magnitude); dashed line in the porous bed is a dividing streamline which separates the interfacial exchange zone from deeper zones dominated by ambient underflow, the vertical distance from the trough of the bedform to the deepest section of this streamline defines the depth of the exchange zone, d_z. (d) Close up view of the eddy showing streamlines. (Simulation for larger $H/L = 0.143$ and smaller $L_c/L = 0.74$ to make eddy more prominent.)

shown to be strictly valid only in porous media whose porosities are of the order of 0.9 or greater [29]. For interfaces with a lower porosity porous media, a no-slip condition for the water column is a valid approximation [44]. In any event, a slip-condition along the SWI would not significantly change the pressure distribution or the interfacial exchange that it controls. The small slip velocities involved would simply be too small. Finally, this set of boundary conditions for the coupled system is an improvement over past practices; most previous studies of interfacial exchange focus only on fluid flow within the sediments and impose an *ab extra*, known-pressure boundary along the SWI [4,18,31,39,42].

To approximate an infinite horizontal domain solution, we impose spatially periodic pressure and velocity boundaries along the vertical sides for both the water column and the sediments (Fig. 1a). The same mean pressure drop, dp, is prescribed between the two vertical boundaries for both domains. Pressure is also specified at the upper right or lower right corner of the NS domain in order to facilitate the periodic boundaries and achieve a unique solution. Ambient flow is always from left to right. Stability and accuracy of the NS solution is ensured via using Lagrange $p2$–$p1$ elements (second order Lagrange elements for velocity and linear for pressure). Similarly, we use second order Lagrange elements for the Darcy domain. The number of triangular elements range from about ~18,000 to near 43,000 depending on dune geometry and hydrodynamic conditions (Fig. 1b). Element distribution is densest at the SWI; and denser in the water column than in the porous bed. The highest resolution is 1 cm. We calculated Kolmogorov microscales to see how much additional effort would be needed to model water-column turbulence by direct numerical simulation of the NS equations. For a bedform Reynolds number (see below) of 10,000 the target grid size would be half a millimeter, 20 times smaller than currently simulated. But such simulations would also need to be three-dimensional and transient, and consequently were beyond the scope of this study. Sensitivity to grid spacing was tested for the laminar flow conditions of this paper, and the presented solutions are converged with respect to the grid.

In order to answer the questions posed in Section 1.2, we ran multiple simulations with different parameters. We varied the bedform length (L), bed crossover length (L_c, the x-location of the crest relative to the entire bedform), bedform height (H), and the depth of impermeable boundary located at the bottom of the sediments (d_b). These parameters are illustrated in Fig. 1a. Several ambient or mean pressure drops (dp) were used to effectively vary the average velocity (U_{ave}) in the water column as well as the Reynolds number (Re). To best characterize the dynamics we define a bedform Reynolds number in terms of the height H as

$$Re = \frac{U_{ave}H}{v} \quad (6)$$

where v is the kinematic viscosity of water at standard conditions (20 °C), and U_{ave} is the characteristic velocity defined as the average velocity along a vertical-section in the water column, taken from the crest of the bedform to the top boundary. Steady-state numerical solution of the Navier-Stokes equations was possible for Re up to ~15,000. Apparently, small perturbations introduced by roundoff and truncation error were damped out by the numerical scheme up to this limit, and the solution produced higher-Re laminar flows. But above this limit small perturbations grew and, for our relatively coarse grid, instead of creating turbulence the solution simply blew up. We limit our results to lower Re where turbulence is less likely to occur in natural flows. Froude numbers (with the water-column depth as the characteristic length) for the water column are $\ll 1$ in all simulations; we did not simulate a free surface at the top of the water column.

Our answers to the questions in Section 1.2 focus on dunes. These ubiquitous larger scale features are expected to have a more profound effect on interfacial exchange than smaller bedforms. Dunes typically, though not strictly, have bedform length (L) greater than 0.6 m and bedform height (H) larger than 0.04 m [51] and are formed under broad hydrodynamic and sedimentological conditions. Fortunately, empirical studies such as by Yalin [51] have delimited stability fields for different bedforms including dunes. These were used as the basis for fixing bedform height ($H = 0.05$ m), and selecting ranges of bedform length (L), steepness (H/L), and asymmetry (L_c/L) for the sensitivity analyses. We chose as the base case for these simulations $H = 0.05$ m, $H/L = 0.05$, and $L_c/L = 0.9$; this is similar to the base case in Cardenas and Wilson [5]. We fixed water-column depth ($d_{wat} = 0.45$ m), but varied the thickness of the sediments (d_b); for the base case d_b=2 m. Southard and Boguchwal [43] demonstrated that dunes do not form in fine sediments ($d_{10} < 0.15$ mm); thus we assigned the sediments for both ripples and dunes an intrinsic permeability value of $k = 1 \times 10^{-10}$ m^2, which is within the range for well-sorted coarse sand. This permeability is small enough to ensure that the flawed boundary conditions at the sediment–water interface will not be seriously violated (e.g., requiring a slip condition and/or having sufficient flux to require perfectly matched fluxes and a fully coupled solution). At the end of the paper we examine a smaller bedform, i.e. ripples, but consider only one bedform geometry (i.e., H, L, H/L, L_c/L, etc. are fixed) and compare to experiments.

3. Results and discussion

3.1. Eddy geometry and bottom pressure distribution

We first study the influence of triangular bedforms on the geometry and size of the water-column eddy that forms downstream of the bedform crest, and the resulting bottom pressures (that drive the flow through the sediments). A typical simulation result is portrayed in Fig. 1c (for a larger dune steepness and smaller asymmetry in order to highlight features; the arrows in the figure indicate only flow direction and not magnitude). The flow in the water-column accelerates on the stoss side and decelerates on the lee side of the bedform. An eddy is visible in the water-column downstream of the bedform crest, as indicated by the arrows. A close up view of the eddy is shown in Fig. 1d, with streamlines instead of velocities in the water column. Fig. 2 provides a view of the pressures and flow fields for the dune base case, over a range of Reynolds numbers (where increasing dp is used to increase U_{ave} and Re). Once again the arrows in the figure only indicate flow direction and not magnitude. At the lowest Re, which is of no practical importance, the water-column flow is creeping and there is no eddy. Above a threshold Re, which depends on the bedform geometry, separation occurs and an eddy forms around the trough. The eddy gets larger as Re increases further. The eddy detachment point (x_d; see Fig. 1d) migrates upstream and up the lee face towards the crest, while the reattachment point (x_r) migrates downstream and up the stoss face (Fig. 2). The eddy size, measured by length $L_e = x_r - x_d$, is particularly sensitive to the current at low Re (Fig. 3a).

Well above the bottom of the water column, the mean pressure gradient in the water column dominates over local pressure gradients generated by the current–bedform interaction (Fig. 2). At the bottom, the pressure is continuous across the sediment–water interface. The eddy detaches from the SWI near the point of minimum local pressure (p_{min}), which is located close to the bedform crest when $Re > 200$, and reattaches near the point of maximum pressure (p_{max}), on the stoss face. Normalized bottom pressures (p*) are plotted in Fig. 4 for the same Reynolds numbers found in Fig. 2. The bottom pressures for any one bedform wavelength are normalized by calculating the midpoint pressure (one half of the sum of p_{max} and p_{min}) and pressure "amplitude" (one half of the difference of p_{max} and p_{min}), then subtracting the midpoint value from the bottom pressure and dividing by the amplitude. For creeping flow the maximum pressure, p^*_{max}, is located near the trough, as one would expect from continuity and the Bernoulli equation. As Re increases, an eddy forms and the location of maximum pressure, which is almost co-located with the reattachment point, migrates downstream. The minimum value of the normalized pressure, p^*_{min}, is located at the crest for creeping flow, and at or just downstream of the crest for higher Res (where it is essentially co-located with the eddy detachment point for higher Res). Approaching this minimum from upstream, there is a significant dip in pressure at or near the crest of the bedform. The pressure then gradually recovers over the bedform lee face and trough.

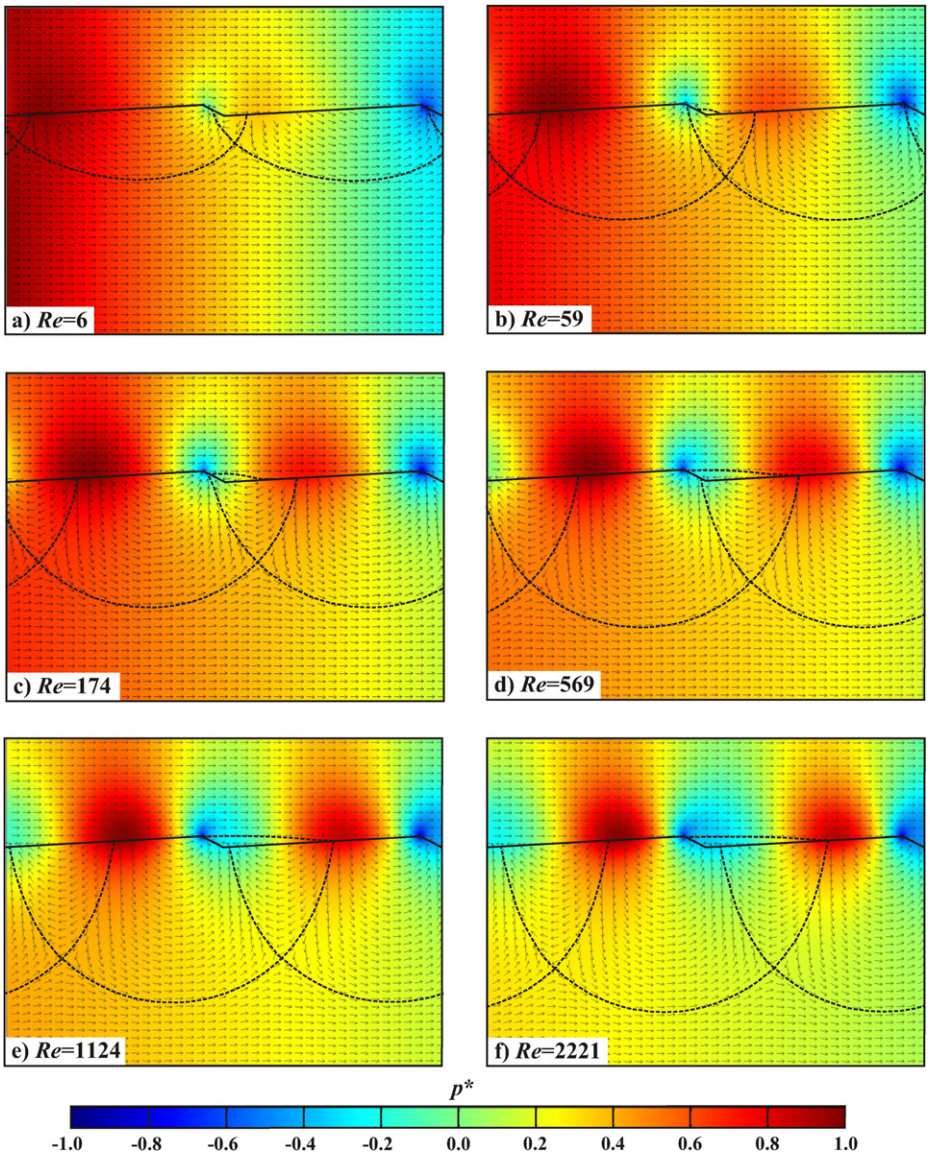

Fig. 2. Typical solutions for normalized pressure (indicated by color spectrum) and flow directions (arrows are of equal lengths and do not indicate magnitude) over and through a dune. Shown are flow fields (a–f) for six Reynolds numbers ($Re = 6$, 59, 174, 569, 1124, 2221) depicting the development of the eddy, and the co-location of eddy reattachment points and pore-water flow divides. Dashed lines are streamlines that divide the porous bed into distinct flow cells ($H = 0.05$ m, $L = 1.0$ m, $H/L = 0.05$, $L_c/L = 0.9$, $d_b = 2.0$ m, $d_{wat} = 0.45$ m, $k = 1 \times 10^{-10}$ m/s). (For interpretation of the references in colour in this figure legend, the reader is referred to the web version of this article.)

3.2. Interfacial exchange zone configuration and flux

Figs. 1 and 2 visually display the relationship between flow conditions above and below the sediment–water interface. Below the SWI, the pore-water flow is controlled by the pressure distribution at the bottom of the water column, which at higher *Re*s is related to eddy size. The pattern of pore-water flow directions in Fig. 2 is indicated by the arrows, which show flow direction (not magnitude). Pore-water flow is into the bed on the upper part of the bedform's stoss face, and back up into the water column on the lee face and the lower part of the stoss face. Further away from the SWI, in the porous bed below, the mean pressure gradient dominates over local gradients. This results in ''underflow'', or ambient flow, within the sediments and is present in all our simulations. The sediments are subjected to the same mean pressure gradient as that in the water column. Also depicted in Fig. 1c is a pore-water streamline (dashed line) which separates the sediments affected by advective interfacial exchange flow (the interfacial exchange zone, IEZ), from the unaffected area dominated by underflow. This streamline is visually picked based on a high-density plot of streamlines. The maximum vertical extent of the IEZ (d_z) is delineated by the deepest portion of this streamline, as defined by the vertical distance between the trough of the bedform to the trough of the dashed line (see also Fig. 2). We use this as a metric for IEZ size, and it increases with *Re* towards some asymptotic limit (Fig. 3a), and is par-

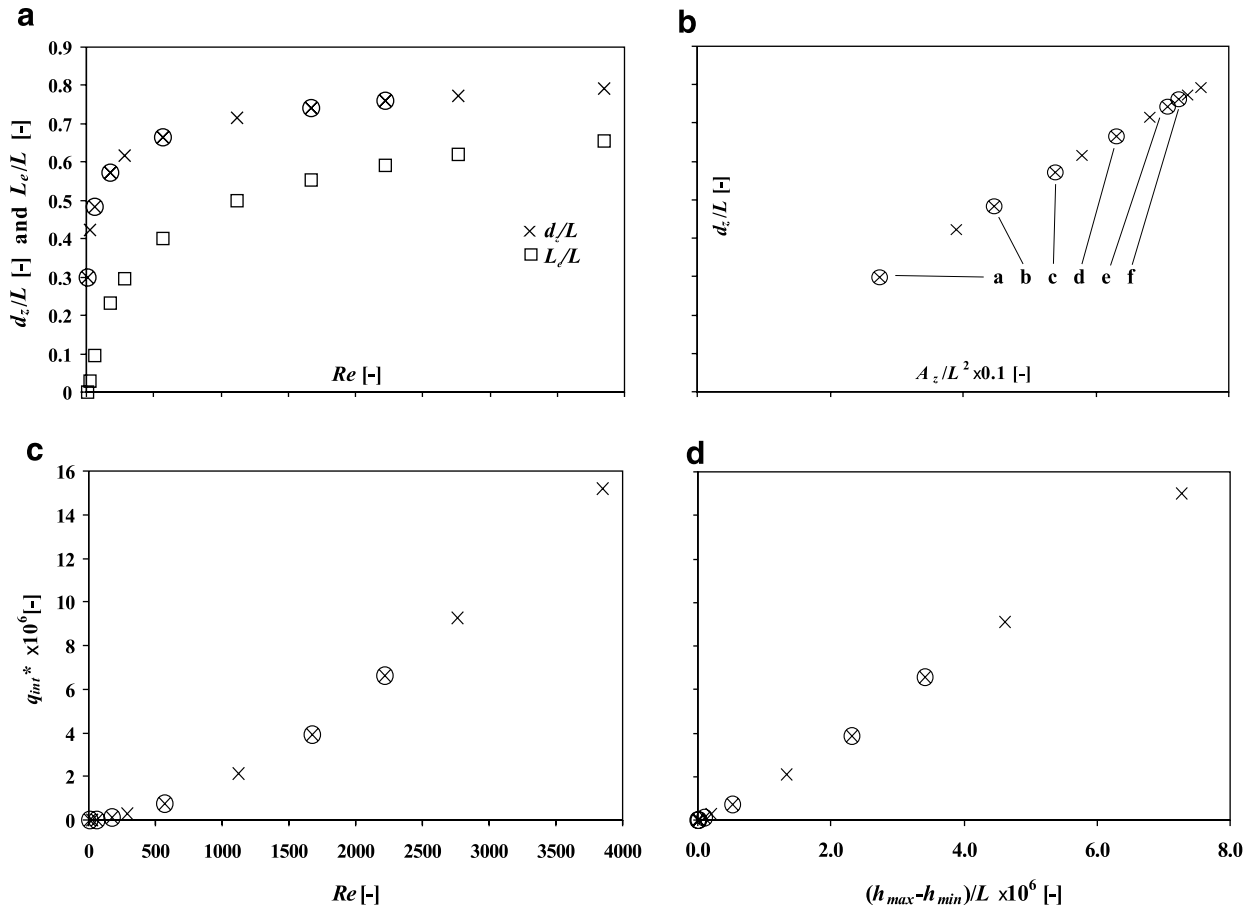

Fig. 3. (a) Relationship of eddy length, L_e (squares), and interfacial exchange zone depth, d_z, (x's) with Re. The horizontal length of the eddy is measured from the detachment to reattachment points, across the trough. (b) Relationship between IEZ depth and area, A_z. (c) Interfacial exchange flux density, q^*_{int} as a function of (c) Re and (d) pressure drop between points of maximum and minimum bottom pressure (where the pressure drop is written in terms of head, $h = p/\rho g$). Conditions used in simulations are the same as in Fig. 2. The six simulations shown in Fig. 2 are indicated by encircled x's and corresponding letter labels in (b).

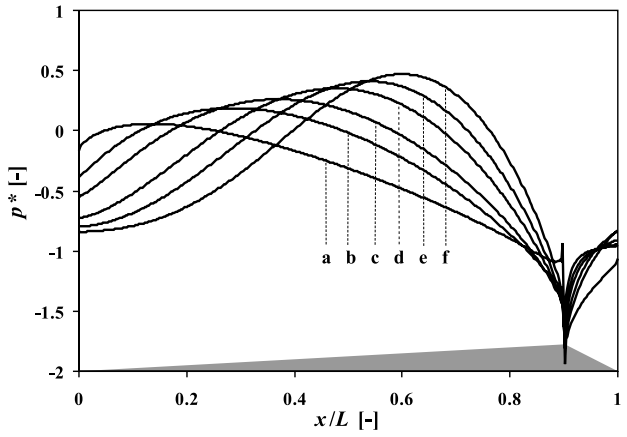

Fig. 4. Simulated pressure (normalized $p*$) profiles for different Re taken along the bed surface for the conditions of Fig. 2 (letter scheme is same as in Fig. 2). Location x is measured downstream from the trough. Gray area illustrates the corresponding bedform geometry.

ticularly sensitive to low Res. Another metric is the area (A_z) of the IEZ, which is the area swept by all water entering the (upper part of the) stoss face of a single bedform. That d_z is a good metric for the IEZ is confirmed by the almost linear relationship between d_z and A_z (Fig. 3b).

The eddy and related bottom pressures determine the flow field in the sediments and the size of the interfacial exchange zone. We demonstrate this first by examining the dependence of the exchange zone depth (d_z) on Re. As shown in Fig. 3a, it is functionally similar to that for the eddy length (L_e). Second, we observe within the sediments that flow divides, which separate the flow cells into one where flow is dominantly upstream and towards the stoss face and one where flow is dominantly downstream and towards the lee face (Fig. 2), essentially coincide with eddy reattachment points for $Re > 200$. These observations demonstrate a direct relationship between flow conditions above and below the SWI. The flow fields also show that flow cells within the bed are not confined to a single bedform, i.e., there is cross-bedform flow. Although we'll see below that the bedform length (L) can be applied as a basic unit for scaling the IEZ, this does not necessarily mean that one bedform is a closed hydrodynamic system where divides coincide with natural boundaries such as crests or troughs.

Another measure of interfacial exchange is the IEZ effective flux density. We compute this as follows: (i) first, we integrate the magnitude of the normal flux over a bedform's surface, L_{int} (Fig. 1b), to get total volumetric flux, and then divide it by the wavelength of the bedform (L) which results in an effective flux density and (ii) then, we divide the effective flux density by two since the integration does not discriminate between flux going in and out of the bed which are equal. The final quantity, q_{int}, is an effective flux density based on the bedform length. We non-dimensionalize q_{int} by dividing by hydraulic conductivity of the sediments, $q^*_{int} = q_{int}/K$ ($K = k\rho g/\mu$, where g is the gravitational constant). The volumetric flux is then given by the product LKq^*_{int}. Fig. 3c and 3d show that the IEZ flux grows with Re and with the difference between maximum and minimum bottom pressures, both without limit. As the current and Re increase the bottom pressure variation increases. It is interesting that these relationships become linear for $Re > 1000$. Of course we would expect a linear relationship between pressure drop and IEZ flux by Darcy's law, if the flow area were not changing. But, as suggested by Figs. 2 and 3a and b, the area is still changing (for $Re > 1000$) and slightly increasing even while the flux appears to have already reached this linear behavior.

Fig. 5 shows two velocity magnitude-depth profiles, one taken vertically through the bed from the crest, and the other from the trough, down to four bedform heights below. Velocity drops exponentially below the bed surface. At the elevation of the bottom of the bedform trough, the velocity below the crest has dropped by about 93%. Vertical profiles taken from the troughs show a similar but not as drastic decrease in velocity. Moreover, the maximum velocity magnitude for the "trough" profile, which like the "crest" profile also occurs along the SWI, is about 5% of the maximum velocity magnitude of the "crest" profile. This relationship, which is observed over a range of Re's, suggests that fast flow and therefore efficient materials cycling is expected to be concentrated within the bedforms. Models that approximate advective exchange through imposing spatially variable pressure on a flat bed surface may be able to correctly simulate deeper portions of the pore-flow field (e.g., [38]), but miss this important aspect.

Before beginning the sensitivity exercise in the next section, we need to know that each simulated domain is deep enough to ensure that the IEZ is not disturbed by the arbitrary location of the porous domain's bottom boundary. We know that if there were no underflow, IEZ depth d_z would be equal to the depth of the lower impermeable boundary, d_b. When underflow is present, such as in our case, d_z is less than d_b, as long as d_b is deep enough. This is illustrated in Fig. 6 for $Re = 1000$. When d_z/d_b is less than about 0.7, the IEZ is essentially independent of d_b. In order to approximate a solution for a vertically infinite bed in the sensitivity simulations, we ensured that $d_z/d_b < 0.7$. (The results in Fig. 6 can also be used as a guide for designing flume experiments and to ensure that boundary effects are minimized. In the next section we'll see that d_z never exceeds L in value; for design purposes this deep-bed criteria can then be conservatively rewritten as $L < 0.7d_b$. This criterion would be even more conservative for ripples, which have a larger H/L.)

3.3. IEZ sensitivity to current and Reynolds Number in the water column

Let's more closely examine how Re affects d_z, the interfacial exchange zone depth, and also q_{int}, the normal flux through the surface of one bedform. This is done by looking at dunes of various geometries found in nature. Our definition of the Reynolds number (6) is convenient since it can be directly tied to IEZ dynamics. For instance, if there is no current, $U_{ave} = 0$, $Re = 0$, and the IEZ will not form. Simply put, there is no pressure gradient along

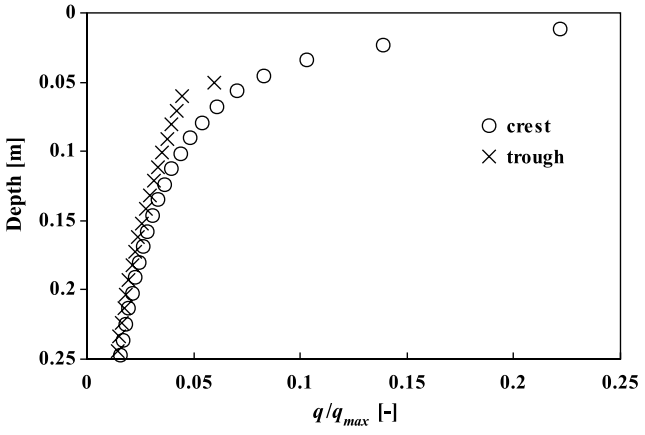

Fig. 5. Depth profiles of normalized magnitudes of pore-water velocities (q is Darcy velocity and q_{max} is maximum velocity just below the interface at the crest) taken below the crest (hollow symbols) and below the trough (solid symbols) for different Res. Depths are taken from the crest. Conditions are the same as in Fig. 2d ($Re = 569$).

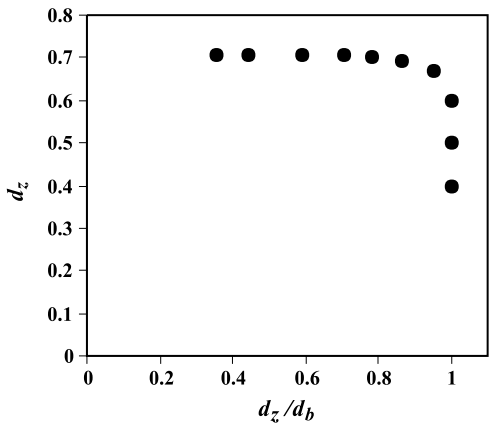

Fig. 6. Plot of interfacial exchange zone vertical extent, d_z [m], versus d_z/d_b with underflow in the sediments. When the depth of the impermeable boundary, d_b, is sufficiently large ($d_z/d_b < 0.7$), the simulated extent d_z approximates that for an infinite bed. Conditions are the same as in Fig. 2 except for variable d_b ($Re = 1000$).

the bed surface set-up by the current–bed topography interactions, such as depicted in Fig. 2, if there is no current. Likewise, we get the same result when $H = 0$ and there is no obstacle or topography. The current induced pressure distribution along the flat surface drops uniformly and linearly, and streamlines in the porous bed are horizontal and parallel to the now flat interface.

We analyzed the impact of Re for different bedform steepnesses or aspect ratios (H/L). Bedform steepness was varied from 0.0385 to 0.0555 following the observations by Yalin [51] that this range for steepness is common for dunes, although there are dunes observed in nature and in lab experiments outside this range. For all the dune bedforms considered, we found that IEZ depth, d_z, increases abruptly when Re is low and eventually becomes asymptotic (as in Fig. 3a). More notable is that when d_z is non-dimensionalized by dividing it by L, the simulation results fall on one curve (Fig. 7a). Dunes, or other bedforms such as ripples, with aspect ratios outside of the range we investigated may fall outside this curve. We fit the following functional model to the dimensionless data in Fig. 7a:

Morgan–Mercer–Flodin model:

$$(d_z/L) = \frac{(ab + cRe^{d})}{(b + Re^{d})} \tag{7}$$

The MMF model [27], which was originally developed to describe the unrelated problem of resource-limited growth rate of higher organisms, fits well. This function behaves such that the dependent variable (d_z/L) is equal to fitting parameter a at the y-intercept and that the asymptotic limit of the dependent variable approaches c as the independent variable (Re) approaches infinity. In our case, a is approximately 0 and c is approximately 1 (see Table 1). In fact, we expect that the curve should pass through the origin ($Re = 0$, $d_z/L = 0 = a$). Thus, we can constrain the MMF model and reduce it to

Michaelis–Menten model:

$$(d_z/L) = \frac{Re^{d}}{b + Re^{d}} \tag{8}$$

which was originally used to describe the kinetics of enzymatically catalyzed reactions [26]. The MM model provides a slightly inferior, yet still excellent, fit (Fig. 7a; Table 1). In both models we find that dune d_z is less than L at all Re's. Since d_z is tied to and behaves similarly as eddy length, L_e, with respect to changes in Re (see previous discussion), this limitation in d_z/L is primarily controlled by the natural limitation on the eddy length which can never be greater than the bedform length. Fitted parameters in Eqs. (7) and (8) are listed in Table 1.

Plotting normalized flux density, q^*_{int}, as a function of Re (Fig. 7b) also results in points essentially lying along one curve, which in this case is described by the power function:

$$q_{int}* = aRe^{b} \tag{9}$$

where $a = 9.78 \times 10^{-11}$ and b = 1.43. Unlike IEZ depth, which follows a saturation growth type model, the IEZ flux increases non-asymptotically with Re (Fig. 7b).

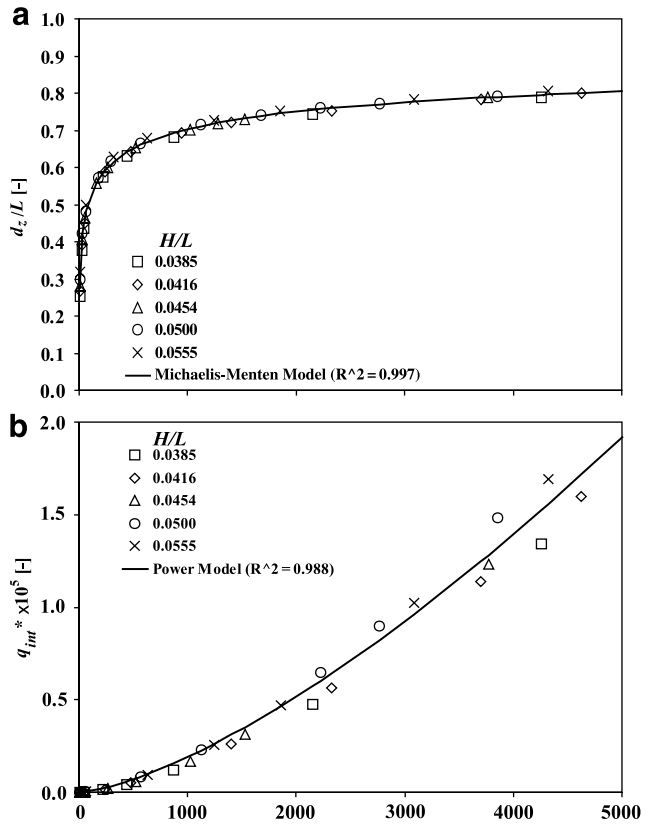

Fig. 7. Dependence of dimensionless exchange depth d_z/L (a) and dimensionless bed-surface exchange flux density q^*_{int} (b) on Re ($L_c/L = 0.9$, $H = 0.05$ m, $k = 1 \times 10^{-10}$ m^2).

3.4. IEZ sensitivity to bedform geometry

Relationships between bedform steepness, H/L, and IEZ depth, d_z/L, and flux, q^*_{int}, are illustrated in Fig. 7. Consider the case where U_{ave} and L are constant; an increase in bedform height (H) increases Re and therefore results in an increase in d_z/L and q^*_{int}. Since L is fixed, the interfacial exchange zone depth and total flux increases with bedform height. Now consider water-column flows with similar Re and therefore similar d_z/L. Assuming U_{ave} and H are constant, the bedform with smaller length (L) will result in a shallower IEZ, as d_z has to be smaller to offset the decrease in L, and a smaller IEZ flux ($= LKq^*_{int}$). Consideration of these relationships, as well as the limiting behavior of L to d_z, suggests that L is an appropriate

Table 1
Results of regression of simulated d_z/L with Re (see Fig. 7 and Eqs. (7) and (8)).

Parameter	MMF	MM
a	−0.0405	–
b	3.9274	4.5158
c	1.0065	–
d	0.3277	0.3429
R^2	0.9970	0.9969

bedform dimension for scaling of IEZ spatial extent. This has direct implications for exchange models that include the area of transient storage zones as a parameter (see Runkel [36], for example). Portions of these areas correspond to "dead zones" in the water column and the rest correspond to IEZs. Knowing a representative value for L could potentially help in the parameterization of this term. Note that this is only valid for cases where the water column is not experiencing a net gain [5] or loss of water through the bed.

We also examined the asymmetry of bedforms as indicated by the ratio of bed crossover length, L_c (see Fig. 1a for illustration), with respect to the entire bedform length, L. Ripples and dunes are typically formed in unidirectional flow and usually have an asymmetry ratio, L_c/L, of 0.7–0.9. Bedforms with an L_c/L that is less than this range are more typical of areas where flow is not dominantly unidirectional (but not necessarily oscillatory), i.e., estuaries or tidal flats. However, such bedforms are also present in rivers. For example, antidunes have an L_c/L less than 0.5. Our results show that at low Re's, IEZ depth, d_z is not very sensitive to L_c/L (Fig. 8a). The sensitivity of d_z to L_c/L increases with rising Re. As Re rises, d_z is smallest at $L_c/L = 0.6$–0.7 and largest at $L_c/L = 0.1$–0.3, for low and intermediate Re, and at $L_c/L = 0.9$, for higher Re. The interfacial-exchange flux density, q^*_{int}, decreases slightly with an increase in L_c/L (Fig. 8b). However, for $L_c/L \geqslant 0.6$, q^*_{int} appears to stabilize. Equilibrium unidirectional bedforms have L_c/L's that are in this range because of drag minimization, with the result that these equilibrium bedforms also minimize advective interfacial exchange.

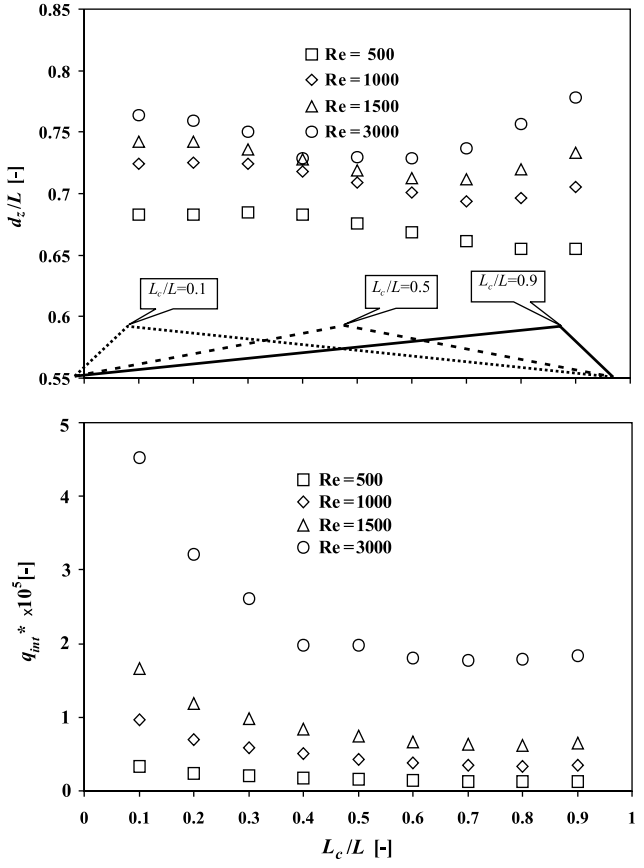

Fig. 8. Effect of bedform asymmetry, L_c/L, on IEZ depth, d_z/L (a) and on IEZ flux density, q^*_{int} (b); in all cases flow is from left to right. ($L = 1.0$ m, $H/L = 0.05$, $H = 0.05$ m, $k = 1 \times 10^{-10}$ m^2.)

4. Limitations and comparison to experiments

The major assumption underlying these simulations is laminar flow in the water column. Where natural flows are characterized by small currents and laminar flow, such as in quiescent lakes, wetlands, or ocean bottoms, our results can be used predictively, but for stronger currents their main power is explanatory. We believe that this power is significant, as demonstrated by the discussion in Section 3. However, most interesting natural flows, and most laboratory experiments, are turbulent. We compare our simulation results to various laboratory flume experiments (e.g., [1,6,41]), most of which involve turbulent flow. While some differences between the simulations and experiments can be attributed to non-ideal conditions in the experiments (several of which we will mention), the major differences are due to the presence of turbulence. We also explore how the laminar flow results can be used to provide estimates of limiting conditions when the water column is turbulent.

4.1. Eddy geometry

The sharp increase in eddy size with Re, which we demonstrate in Fig. 3a, is well known for laminar flow past a backward-facing step. Armaly et al. [1] found this behavior for Re's of 0–600, where we have converted their result to a more compatible Re (defined by the mean velocity over the step and the step height). The eddy zone behind the backward-facing step then starts to shrink (in a step-wise fashion) as the flow becomes transitional, at Re's of 600–3300. After the eddy achieves a minimal size, it slightly grows again with even higher Res up to a stable size for fully turbulent flow at $Re > 3300$. The turbulent eddy is smaller than the maximum achieved under laminar flow conditions (in [1] it is less than half the size of the size of the largest laminar eddy). We ran additional triangular bedform simulations for higher Re's than shown in Figs. 2, 3, and 7, but it becomes apparent that, without explicit consideration for turbulence, the simulated eddy attains a maximum size and never decreases. Experiments (e.g., [6,12,28]) for fully turbulent flow over two-dimensional triangular bedforms (there are no published results for laminar or transitional flows) result in smaller eddies that reattach at points closer to the trough than the laminar flow results presented here, consistent with [1]'s results for the backward-facing step. Extrapolating from the backward-facing step results, we suggest that the point at which the rate of increase in eddy size with Re starts to decreases significantly (Fig. 3a) can be loosely interpreted as the limit at which the flow becomes transitional from laminar. In the case of the simulations in Fig. 3 or 7, this limit is roughly in the Re range of

600–900. It might be on the high side of this range, as we expect the eddy growth rate to decrease earlier in our case compared to a back-step, due to the finite amount of space that the eddy can occupy with periodic bedforms. A universal threshold *Re* between laminar-transitional-turbulent flow regimes for triangular bedforms is not well-documented. Defining a threshold becomes more difficult when multiple geometries (e.g., several H/L and L_c/L values) are considered, such as our case. In this paper we present results at higher *Re*'s (e.g., Fig. 7) for these reasons as well as for completeness. Additionally, presenting results through the transitional regime facilitates comparison with similar future multiphysics studies that consider transitional and/ or turbulent flows in the water column.

4.2. Bottom pressure

Because of its typically smaller eddy size, turbulent flow in the water column will have a somewhat different pressure distribution along the SWI compared to our laminar flow solution of the NS equations. The differences are elucidated in Fig. 9 where normalized bottom pressures are plotted for a bedform conforming to the geometry of ripples, both in size (H and L), steepness (H/L) and asymmetry (L_c/L). The normalization is similar to that in Fig. 4, except that the mean pressure gradient is also removed [10]. The plot includes Elliott and Brooks' [10,12] fit of fully turbulent flow pressure measurements that were taken on similar experimental impermeable triangular ripple bedforms by Fehlman [13,41]. It also includes new laminar flow simulations of this geometry for various *Re* (see the figure caption for the simulated parameter values). The Fehlman pressure profile (gray line) has a maximum that is closer to the trough than the simulated ($Re > 200$) laminar flow results (Fig. 9), consistent with a smaller eddy for turbulent flow. Unlike the simulations, the gray line does not have a dip in pressure at or near the crest of the bedform. Instead, the low pressure zone corresponds to a broad area encompassing the trough of the bedform. This is an experimental artifact, as a pressure dip or adverse pressure gradient is necessary for flow to separate and reverse; it is difficult or impossible to resolve the dip in flume experiments. (Pressure probes need to be accurately placed where the reattachment point is located but this is not known *a priori*. Even if probe placement were optimal, the time-averaging needs to be carefully considered [8].) Other studies show disparate results. For example, Raudkivi [34] found that pressure dips near the crest then increases through the lee face of the triangular bedform; Yoon and Patel [52], using a Reynolds averaged NS model of the water column, also found a similar upward trend in pressure on the lee face. A large gradient in pressure at the lee face of a triangular mound was observed by Huettel and Gust [21]. On the other hand, the observations and calculations in Vanoni and Hwang [47] and Mendoza and Shen [25] have more or less similar trends with those of the gray curve in Fig. 9. Nonetheless, our results, as well as those of the studies mentioned, consistently show the location of the lowest pressure at or near the crest. In some it is a dominant trough and in others a broad area. The differences are due to experimental design and flow conditions, i.e., laminar to transitional to turbulent. The *Re*s for the references we cite vary from about 3000 to as high as 50,000, higher than in the simulations presented here. While the simulations show that for laminar flow the normalized pressure profiles are sensitive to *Re* (Figs. 4 and 9), sensitivity to *Re* is expected to be much less for turbulent flow conditions (e.g., [13,41,47]).

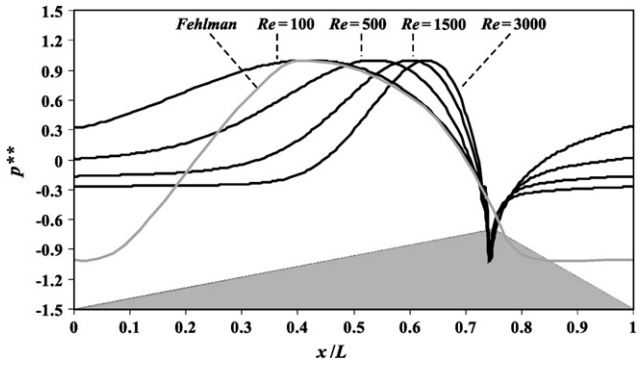

Fig. 9. Simulated pressure (normalized p^{**}, where p^{**} is normalized similar to p^*, Section 3.1, except that the ambient gradient is removed) profiles for different *Re* taken along the bed surface for a ripple bedform [11]; gray line corresponds to normalized pressure distribution based on measurements by Fehlman [13] over a similar bedform, as presented in [11] ($L = 0.178$ m, $L_c = 0.132$ m, $H = 0.0254$ m, $H/L = 0.143$, $d_b = 0.135$ m, $d_{wat} = 0.0645$ m, $k = 2 \times 10^{-10}$ m^2).

4.3. Discussion

The limitations of our formulation, especially the assumption of laminar water-column flow, should be considered when interpreting our findings. Despite this, our results help us understand how IEZs develop in these systems and provide a foretaste for future studies that explicitly account for turbulence. They also provide guidelines that we can use to estimate limiting conditions of interest when the flow is turbulent. For example, the laminar flow model projects a maximum IEZ depth, d_z, approaching the bedform length, L; this discussion suggests that under fully turbulent flow the IEZ depth will be considerably smaller, closer to $0.5L$, and much less sensitive to *Re*. The maximum IEZ depth, for any flow condition, will occur when laminar flow begins its transition to turbulent flow, expected to occur below $Re = 1000$. This maximum depth cannot be greater than $0.7L$. Under fully turbulent flow the size of the eddy and details of the bottom-pressure distribution will change, but the IEZ shape should be qualitatively similar to that shown in Fig. 2 (based on *Re*s in Fig. 9 and the discussion of the eddy for the backward facing step). The pressure difference in turbulent flow will be substantially greater than computed here, and fluxes will be substantially larger. Fig. 7b then becomes a lower-bound estimate of flux, but the figure also suggests that

we should expect an almost linear growth of flux with *Re* under turbulent flow.

5. Summary

Using a sequential numerical formulation we modeled coupled flow above and below two-dimensional bedforms on a sediment–water interface. The water column above the interface is governed by the viscous-flow Navier-Stokes and continuity equations while the porous bed follows the groundwater flow equation. FEMLAB (now called COMSOL Multiphysics), a multiphysics finite element analysis software, was used to solve the governing equations. We show, for laminar flow in the water column, how the relationship between driving forces and resulting flow fields and fluxes change across evolving dynamical settings.

Coupling between water column and exchange zone flow is mainly controlled by the behavior of the eddy in the water column. In fact, the deepening of the exchange zone with increasing Reynolds number mirrors the growth of the eddy. The eddy detaches near where the minimum pressure is located along the interface and reattaches close to the location of maximum pressure. These two critical pressures, which determine maximum pressure gradient, dominantly control the exchange zone flow field. The simulations show that the water-column eddy size and reattachment point position controls the location of flow divides within the porous bed. Since eddy size increases with an increase in Reynolds number, the same dynamic behavior is observed in the geometry and flow field of the interfacial exchange zone. Flow divides within the bed do not necessarily correspond to natural breaks such as bedform troughs and crests. Some flow cells cross bedforms illustrating that a bedform is not necessarily a closed hydrodynamic system. Lastly, pore-water velocities drop significantly with depth from the bed surface. Pore-water velocities near the trough are lower than those near the crest. These results support the importance of and the need for hydrodynamic models that explicitly consider the geometry of bedforms.

The plot of interfacial exchange zone depth as a function of water column Reynolds number is described by a simple function, the Michaelis–Menten model, with a single curve for a range of common dune steepnesses. That the depth is a good metric of the interfacial exchange zone is shown by the linear relationship between exchange zone area and depth. The interfacial exchange zone is very sensitive to lower Reynolds numbers, but at higher Reynolds numbers stabilizes at a depth that is equivalent to the length of the bedform. This information is potentially useful in the parameterization of the interfacial exchange zone area, which is commonly included in transient storage models. The relationship between bed-surface flux and Reynolds number is described by a non-asymptotic power function. Flux is mainly controlled by the pressure gradient set-up along the bed surface due to current–bedform interactions. At higher Reynolds numbers the exchange zone depth and area are less sensitive to the pressure gradient, and the exchange zone flux is linearly related to Reynolds number owing to Darcy's Law.

Aside from demonstrating the effects of bedform height and length, the results show that both interfacial exchange zone depth and bed fluxes may change with the relative location of the bedform crest. At low Reynolds number, the interfacial exchange zone depth is not affected much by the relative location of the crest but it becomes more sensitive to the crest location as the Reynolds number increases. Fluxes are higher when the crest is further upstream from the downstream-located trough. Changes to flux are minimized and appear to stabilize as the crest gets closer to the downstream trough.

The laminar flow results also provide guidelines that we can use to address turbulent flow conditions. For example, once we take into account our well-founded speculation that the IEZ depth and configuration will be relatively insensitive to *Re* under fully turbulent flow conditions, we believe that most of the qualitative conclusions from this summary will still hold. We can even use the laminar flow results as limiting conditions to quantitative behavior, for example, suggesting that the IEZ will never get larger that $0.7L$, under any condition, and that in fully turbulent conditions its depth will be more like $0.5L$.

What these laminar flow results lack in predictive ability they make up for in explanatory power and, in any event, will help design future studies that directly address turbulence and other issues. Throughout the development of fluid mechanics laminar-flow studies have played this pioneering role.

Acknowledgements

MBC was supported by the Frank E. Kottlowski Fellowship of the New Mexico Bureau of Geology and Mineral Resources at the New Mexico Institute of Mining and Technology (NMIMT) during the duration of this study. Computing resources were provided by the Department of Earth and Environmental Sciences at NMIMT. We are grateful for the support by technicians at Comsol. Drafts of this manuscript benefited from comments from Glenn Spinelli, Markus Huettel and four anonymous reviewers.

References

[1] Armaly BF, Durst F, Pereira JCF, Schonung B. Experimental and theoretical investigation of backward-facing step flow. J Fluid Mech 1983;127:473–96.

[2] Boudreau BP. Solute transport above the sediment–water interface. In: Boudreau BP, Jorgensen BB, editors. The benthic boundary layer: transport processes and biogeochemistry. New York: Oxford University Press; 2001.

[3] Burnett WC, Bokuniewicz H, Huettel M, Moore WS, Taniguchi M. Groundwater and pore water inputs to the coastal zone. Biogeochemistry 2003;66:3–33.

[4] Cardenas MB, Wilson JL, Zlotnik VA. Impact of heterogeneity, bedform configuration, and channel curvature on hyporheic

exchange. Water Resour Res 2004;40:W08307. doi:10.1029/2004WR003008.
[5] Cardenas MB, Wilson JL. The influence of ambient groundwater discharge on hyporheic zones induced by current–bedform interactions. J Hydrology, in press.
[6] Cheong HF, Xue H. Turbulence model for water flow over two-dimensional bedforms. J Hydraul Eng 1997;123(5):402–9.
[7] Choe KY, Gill GA, Lehman RD, Han S, Heim WA, Coale KH. Sediment–water exchange of total mercury in the San Francisco Bay-Delta. Limnol Oceanogr 2004;49(5):1512–27.
[8] Chun S, Liu YZ, Sung HJ. Wall pressure fluctuations of a turbulent and reattaching flow affected by an unsteady wake. Exp Fluids 2004;37:531–46.
[9] Davis TA. A column pre-ordering strategy for the unsymmetric-pattern multifrontal method. ACM Trans Math Software 2004;30(2):165–95.
[10] Elliott AH. Transfer of solutes into and out of streambeds. Ph.D. thesis, Rep KH-R-52, WM Keck Lab of Hydraul and Water Resour, Calif Inst of Technol, Pasadena; 1990.
[11] Elliott AH, Brooks NH. Transfer of nonsorbing solutes to a streambed with bedforms: theory. Water Resour Res 1997;33(1):123–36.
[12] Elliott AH, Brooks NH. Transfer of nonsorbing solutes to a streambed with bedforms: laboratory experiments. Water Resour Res 1997;33(1):137–1151.
[13] Fehlman HM. Resistance components and velocity distributions of open channel flows over bedforms. M.S. Thesis, Colo State Univ, Fort Collins, CO; 1985.
[14] Findlay S. Importance of surface-subsurface exchange in stream ecosystems: the hyporheic zone. Limnol Oceanogr 1995;40(1):159–64.
[15] Harvey JW, Fuller CW. Effect of enhanced manganese oxidation in the hyporheic zone on basin-scale geochemical mass balance. Water Resour Res 1998;34(4):623–36.
[16] Ho RT, Gelhar LW. Turbulent flow with wavy permeable boundaries. J Fluid Mech 1973;58(2):403–14.
[17] Huettel M, Roy H, Precht E, Ehrenhauss S. Hydrodynamical impact of biogeochemical processes in aquatic sediments. Hydrobiologia 2003;494:231–6.
[18] Huettel M, Ziebis W, Forster S, Luther III GW. Advective transport affecting metal and nutrient distributions and interfacial fluxes in permeable sediments. Geochim Cosmochim Acta 1998;62(4):613–31.
[19] Huettel M, Webster IT. Pore-water flow in permeable sediments. In: Boudreau BP, Jorgensen BB, editors. The benthic boundary layer: transport processes and biogeochemistry. New York: Oxford University Press; 2001.
[20] Huettel M, Ziebis W, Forster S. Flow-induced uptake of particulate matter in permeable sediments. Limnol Oceanogr 1996;41(2):309–22.
[21] Huettel M, Gust G. Impact of bioroughness on interfacial solute exchange in permeable sediments. Mar Ecol Prog Ser 1992;89:253–67.
[22] Jorgensen BB, Boudreau BP. Diagenesis and sediment–water exchange. In: Boudreau BP, Jorgensen BB, editors. The benthic boundary layer: transport processes and biogeochemistry. New York: Oxford University Press; 2001.
[23] Kasahara T, Wondzell SM. Geomorphic controls on hyporheic exchange flow in mountain streams. Water Resour Res 2003;39(1):1005. doi:10.1029/2002WR001386.
[24] Marion A, Bellinello M, Guymer I, Packman A. Effect of bedform geometry on the penetration of nonreactive solutes into a streambed. Water Resour Res 2002;38(10):1209. doi:10.1029/2001WR000264.
[25] Mendoza C, Shen HW. Investigation of turbulent flow over dunes. J Hydr Eng ASCE 1990;116(4):459–77.
[26] Michaelis L, Menten ML. Die kinetik der invertinwirkung (The kinetics of invertase activity). Biochem Z 1913;49:333–69.
[27] Morgan PH, Mercer LP, Flodin NW. General model for nutritional responses of higher order mechanisms. Proc Natl Acad Sci USA 1975;72(11):4327–31.
[28] Nelson JM, Smith JD. Mechanics of flow over ripples and dunes. J Geophys Res 1989;94(C6):8146–62.
[29] Nield DA. The limitations of the Brinkman–Forcheimer equation in modeling flow in a saturated porous medium and at an interface. Int J Heat Fluid Flow 1991;12(3):269–72.
[30] Packman AI, Salehin M, Zaramella M. Hyporheic exchange with gravel beds: basic hydrodynamic interactions and bedform-induced advective flows. J Hydr Eng 2004;130(7):647–56.
[31] Packman AI, Brooks NH. Hyporheic exchange of solutes and colloids with moving bedforms. Water Resour Res 2001;37(10):2591–605.
[32] Packman AI, Bencala KE. Modeling surface–subsurface hydrological interactions. In: Jones JB, Mulholland PJ, editors. Streams and ground waters. San Diego: Academic Press; 2000.
[33] Precht E, Huettel M. Advective pore-water exchange driven by surface gravity waves and its ecological implications. Limnol Oceanogr 2003;48(4):1674–84.
[34] Raudkivi AJ. Study of sediment ripple formation. J Hydr Div ASCE 1963;89(6):15–33.
[35] Riedl RJ, Huang H, Machan R. The subtidal pump: A mechanism of interstitial water exchange by wave action. Mar Biol 1972;13:210–21.
[36] Runkel RL. One dimensional transport with inflow and storage (OTIS): a solute transport model for streams and rivers. U.S. Geological Survey Water-Resources Investigation Report 98-4018, Denver: USGS; 1998.
[37] Runkel RL, McKnight DM, Rajaram H. Preface: modeling hyporheic zone processes. Adv Water Resour 2003;26(9):901–5.
[38] Rutherford JC, Boyle JD, Elliott AH, Hatherell TVJ, Chiu TW. Modeling benthic oxygen uptake by pumping. J Environ Eng 1995;121(1):84–95.
[39] Salehin M, Packman AI, Paradis M. Hyporheic exchange with heterogeneous streambeds: laboratory experiments and modeling. Water Resour Res 2004;40:W11504. doi:10.1029/2003WR002567.
[40] Savant SA, Reible DD, Thibodeaux LJ. Convective transport within stable river sediments. Water Resour Res 1987;23(9):1763–8.
[41] Shen HW, Fehlman HM, Mendoza C. Bedform resistances in open channel flows. J Hydr Eng ASCE 1990;116(6):799–815.
[42] Shum KT. Wave-induced advective transport below a rippled water–sediment interface. J Geophys Res 1992;97(C1):798–808.
[43] Southard JB, Boguchwal LA. Bed configurations in steady unidirectional flows. Part 2. Synthesis of flume data. J Sediment Petrol 1990;60(5):658–79.
[44] Tachie MF, James DF, Currie IG. Velocity measurements of a shear flow penetrating a porous medium. J Fluid Mech 2003;493:319–43.
[45] Thibodeaux LJ, Boyle JD. Bedform-generated convective-transport in bottom sediments. Nature 1987;325:341–3.
[46] Triska FJ, Kennedy VC, Avanzino RJ, Zellweger GW, Bencala KE. Retention and transport of nutrients in third-order stream in Northwestern California: Hyporheic processes. Ecology 1989;70(6):1893–905.
[47] Vanoni VA, Hwang LS. Relation between bedforms and friction in streams. J Hydr Div ASCE 1967;93(3):121–44.
[48] Vittal N, Rangu Raju KG, Garde RJ. Resistance of two-dimensional triangular roughness. J Hydr Res 1977;15(1):19–36.
[49] Webb JE, Theodor J. Irrigation of submerged marine sands through wave action. Nature 1968;220:682–5.
[50] Worman A, Packman AI, Johansson H, Jonsson K. Effect of flow-induced exchange in hyporheic zones on longitudinal transport of solutes in streams and rivers. Water Resour Res 2002;38(1). doi:10.1029/2001WR000769.
[51] Yalin MS. Mechanics of sediment transport. second ed. Oxford: Pergamon Press; 1977.
[52] Yoon JY, Patel VC. Numerical model of turbulent flow over sand dune. J Hydr Eng ASCE 1996;122(1):10–8.